TASCC-P-95-3

tascc

Space-time characteristics of fragment emission in the $E / A = 30$ MeV ^{129}Xe + ^{nat}Cu reaction

D.R. Bowman[a], N. Colonna[b], W.A. Friedman[c], L. Celano[b], M. D'Agostino[d],
J.D. Dinius[e], A. Ferrero[f,1], C.K. Gelbke[e], T. Glasmacher[e], D.O. Handzy[e], D. Horn[a],
W.C. Hsi[e], M. Huang[e], I. Iori[f], M.A. Lisa[e,2], W.G. Lynch[e], G.V. Margagliotti[g],
P.M. Milazzo[d], C.P. Montoya[e], A. Moroni[f], G.F. Peaslee[e,3], L. Phair[e,2],
F. Petruzzelli[f], R. Scardaoni[f], C. Schwarz[e,4], M.B. Tsang[e] and C. Williams[e]

[a]AECL Research, Chalk River Laboratories, Ontario, Canada K0J 1J0
[b]INFN, Via Amendola 173, 70126 Bari, Italy
[c]Department of Physics, University of Wisconsin, Madison, Wisconsin 53706 U.S.A.
[d]Dipartimento di Fisica and INFN, Via Irnerio 46, 40126 Bologna, Italy
[e]NSCL, Michigan State University, E. Lansing, Michigan 48824 U.S.A.
[f]Dipartimento di Fisica and INFN, Via Celoria 12, 20133 Milano, Italy
[g]Dipartimento di Fisica and INFN, Via A. Valerio 2, 34127 Trieste, Italy

Sw 9512

---

[1] On leave from the Comisión de Energia Atómica, Argentina
[2] Present address: Lawrence Berkeley Laboratory, 1 Cyclotron Rd., Berkeley, CA 94720 U.S.A.
[3] Present address: Physics Department, Hope College, Holland, MI 49223 U.S.A.
[4] Present address: Gesellschaft für Schwerionenforschung, D-6100 Darmstadt, Germany

Submitted to Phys. Rev. C

NOTICE

Physical and Environmental Sciences
Chalk River Laboratories
Chalk River, ON K0J 1J0 Canada

1995 February

ABSTRACT

Intermediate-mass-fragment emission has been studied in central E/A = 30 MeV ^{129}Xe + ^{nat}Cu reactions. The measured fragment multiplicities, reduced-velocity correlation functions, and emission velocities have been compared with schematic three-body trajectory calculations and with three statistical models with input based upon a dynamical BNV code. The statistical models which include expansion either explicitly or implicitly are able to generate a sufficient number of fragments. The three-body trajectory calculations indicate a mean emission time of ≈ 200 fm/c, consistent with sequential decay. Dynamical Expanding-Emitting Source calculations predict a similiar time scale for fragment emission, and give satisfactory agreement with the experimental correlation functions if the experimental angular distributions are incorporated into the model. The Berlin Multifragmentation Model gives good agreement with the experimental charge distributions, and, depending upon the choice of radius parameter, can provide agreement with either the correlation functions or the fragment emission velocities, but not with both simultaneously. Although an overall good agreement is obtained in the statistical model comparisons, even in the most violent collisions the angular distributions and fragment emission velocities are incompatible with completely-equilibrated decay from a single source.

Typeset using REVTEX

---

[1] On leave from the Comisión de Energia Atómica, Argentina

[2] Present address: Lawrence Berkeley Laboratory, 1 Cyclotron Rd., Berkeley, CA 94720, USA

[3] Present address: Physics Department, Hope College, Holland, MI 49223, USA

[4] Present address: Gesellschaft für Schwerionenforschung, D-6100 Darmstadt, Germany

I. INTRODUCTION

Studies of IMF (intermediate mass fragment; $3 \leq Z \leq 20$) emission [1–50] have provided a wealth of information about the space-time extent of excited nuclear systems. At high bombarding energy, $E/A > 100$ MeV, the fragments appear to be emitted on the very short time scale implied by a prompt multifragment disassembly of heated and expanded nuclear systems [20,21]. At low bombarding energy, $E/A < 20$ MeV, standard compound nucleus decay accounts for much of the fragment yield following either complete or incomplete fusion reactions [33–35]. To gain a systematic understanding of the interaction between complex nuclei it is important to characterize the intermediate bombarding energy regime, where the fragment emission time scale changes from sequential to simultaneous [24,27], and nuclear expansion begins to occur [39,40].

Observables which have been employed to infer the spatial and temporal extensions of fragmentation sources are: fragment yields, fragment-fragment reduced-velocity correlation functions, and emission velocities of emitted fragments. The IMF yields calculated with statistical emission models are strongly dependent on the density of the emitting system [41–44]. Comparisons of experimental data with model predictions have shown that nuclear expansion is needed to reproduce the observed fragment multiplicities and charge distributions, even at bombarding energies as low as $E/A = 35$ MeV [43]. The fragment emission time scale, as determined from fragment-fragment correlations, is a direct measure of the space-time extent of the source [18–32]. The fragment emission velocities are sensitive to an expansion of the source, which leads to a decrease in the Coulomb repulsion energy [40]; and to a collective radial velocity, which provides a boost to the emitted fragments [47,48]. Simultaneous measurements of the relative-velocity correlation functions and the fragment emission velocities may allow a distinction between the spatial and temporal extentions of the source [30].

Both equilibrium and non-equilibrium mechanisms contribute to the measured fragment yield at intermediate bombarding energy (20 MeV $\leq$ E/A $\leq$ 100 MeV) [22,35–38]. Results of microscopic transport model calculations for A $\sim$ 200 systems at bombarding energies E/A $<$ 50 MeV indicate that peripheral collisions lead to projectile- and target-like primary fragments through incomplete damping of the entrance-channel kinetic energy, whereas central collisions lead to a composite system through a fusion-like process [51,52]. Studies of these reactions with state-of-the-art 4π detector systems that allow an approximate impact-parameter selection may be able to identify which reaction mechanisms dominate IMF production for different collision geometries. Such a study was performed for E/A = 35 MeV ^{36}Ar + ^{197}Au reactions [22]. Although contributions from non-equilibrium emission were found to persist in even the most violent collisions, a much larger degree of equilibration was observed as the centrality of the reaction increased.

In this paper we report on a study of the E/A = 30 MeV ^{129}Xe + ^{nat}Cu system with a low-threshold, 4π detector system which allows an event-by-event impact-parameter estimation and has a high efficiency for fragment detection. We primarily confine ourselves to the most violent events where the kinetic energy dissipation and the degree of equilibration is expected to be highest. In contrast to analyses which have focussed on one particular aspect of fragment emission, we examine the three observables described above: the IMF multiplicity and charge distributions, the fragment-fragment reduced-velocity correlation function, and the velocity distributions of fragments with Z=6. We compare the data with predictions of a schematic three-body trajectory calculation, and with three statistical-decay models which make varying assumptions about the characteristics of the decaying system. It is our expectation that no single model with one set of input parameters will successfully predict all of the features of fragment emission, but that important ingredients in each of the models may be brought forth. Our procedure gives a perspective which is perhaps more balanced than studies focussing on a single aspect of a reaction.

The paper is organized as follows: the experimental details are given in Section II, the model calculations are described in Section III, the results are presented and discussed in

Section IV, and a summary is given in Section V.

II. EXPERIMENTAL DETAILS

An E/A = 30 MeV ^{129}Xe beam of intensity ~3 x 10^7 particles/s was delivered by the K1200 Cyclotron of the National Superconducting Cyclotron Laboratory at Michigan State University and impinged upon a target of ^{nat}Cu of 2.4 mg/cm^2 areal density. Charged reaction products were detected from 8° - 23° with 36 elements of the high-resolution gas-Si-Si(Li)-CsI MULTICS array [53], and from 23° - 160° with 158 elements (Rings #3 - #11) of the MSU Miniball [54]. The complete detector system covered a solid angle greater than 87% of 4π.

Charged particles of $1 \leq Z \leq 54$ were detected with the MULTICS array. Detection thresholds were approximately E/A = 2.5 MeV for all fragments, and the resolution in Z was better than 1 unit for $Z < 30$. Energy calibrations were performed by directing 18 separate beams into each of the 36 telescopes [55]. The calibration beams had energies of E/A = 30 and 70 MeV, and ranged in mass from ^{12}C to ^{129}Xe. An energy resolution of better than 2% was obtained. Position calibrations of the Si elements of the MULTICS array were performed with the procedure of ref. [56]. The angular resolution was estimated to be ≈ 0.2 °.

Charged particles of $1 \leq Z \leq 20$ were detected with the Miniball. Identification thresholds were approximately E/A = 2, 3 and 4 MeV for fragments with Z = 3, 10, and 18 fragments, respectively. The resolution in Z was much better than 1 unit for $Z < 6$, and typically ±1 unit for $7 \leq Z \leq 20$. Charged particles with $E/A > 1$ MeV were detected but not identified. Detectors at angles $\theta > 100°$ were covered by 5.05 mg/cm^2 Pb-Sn foils for electron suppresion; these foils increased the energy thresholds by approximately 20%. During the experiment the Miniball was cooled and temperature-stabilized. Drifts in the phototube gains were monitored with a light-pulser system and found to be less than 2%. Absolute energy calibrations were obtained by normalizing the measured proton punch-through points of 75.2 MeV to existing calibration curves [57]. The energy calibrations were estimated to be accurate to ~10% at forward angles where the punch-through points were well identified, and accurate to ~20% for more backward ($\theta > 80°$) angles where they were not.

Data were taken on two conditions: (i) at least two Miniball elements were triggered, or (ii) at least one fragment of $Z > 2$ was detected in the MULTICS array. More than 92% of the events that satisfied condition (ii) also satisfied condition (i). Because of the low beam intensity, the random coincidence rate from different events was less than 0.1%. Events which satisfied either of the two conditions were written to magnetic tape in an event-by-event format. Calibrations were performed off-line, and the results written in an event-by-event sequence to new tapes with parameters of Z, energy, θ, and ϕ.

III. MODELS EMPLOYED

To test the statistical emission hypothesis, we have compared the experimental data with predictions from three statistical-decay codes, each of which rely on different assumptions about the space-time characteristics of the fragmenting system. Rather than attempting to fit the data by choosing optimal values for the many parameters in these models, we have used a set of reasonable and consistent assumptions for each calculation. Our procedure is described in this section.

The code GEMINI [35] calculates sequential binary emission of all species ranging from nucleons to symmetric fission fragments. Light particles are treated with the evaporation formalism [58] and fragments of $Z > 2$ with the transition state model of ref. [59]. There are no three-body correlations in the GEMINI. Each binary decay product is assumed to be fully accelerated by the Coulomb field of its partner before the succeeding particle or fragment is emitted. Therefore, the calculated fragment-fragment reduced-velocity correlation function, which tests the space-time extent of the emitting source, should not be thought of as a realistic prediction for sequential binary decay, but rather as a limit for an infinite time between steps in the decay chain.

The Expanding-Emitting Source Model (EES) of Friedman [60] treats surface evaporation of light particles and fragments ($Z \leq 9$) with the binary evaporation formalism. Both emission probabilities and expansion or contraction of the source are calculated as a function of time. An effective compressibility is built into the model through the following relationship between binding energy and density:

$$E(\rho)/A = E_{LD}(\rho_0)/A + (K/18)(1 - (\rho/\rho_0))^2. \tag{1}$$

Here $E_{LD}(\rho_0)/A$ is the binding energy at normal nuclear density. We choose the finite-nucleus compressibility K to be 144 MeV. This corresponds to a"soft equation-of-state."

The Berlin Multifragmentation Model (BMM) [61] calculates the simultaneous statistical disassembly of a nuclear system inside a volume characterized by a radius $R_{FO} = r_0 A^{1/3}$. Typically the parameter r_0 is set to be approximately 2.1 fm. In one set of calculations, r_0 was increased to 2.6 fm to provide agreement with fragment-fragment correlation functions measured in peripheral reactions at E/A = 50 MeV. [29].

To estimate of the properties of an equilibrated source, we have used the BNV (Boltzmann-Nordheim-Vlasov) model of ref. [63] to simulate the early dynamical stage of the collision [43–46,51,52]. The BNV model allows for pre-equilibrium emission of light particles which can decrease the excitation energy in the residue [49,62]. Calculations at an impact parameter of b=0 fm were followed to times of 140 fm/c [1]. An infinite nuclear matter compressibility K_∞ of 200 MeV was used in these calculations. This also corresponds to a "soft equation-of-state." The mass loss, source density, excitation energy, and collective radial energy [45] predicted by the BNV calculation are shown as a function of time in Fig. 1.

The source properties for GEMINI and the EES model were determined at the time when the nuclear matter returned to normal density following compression (≈80 fm/c). Since these models assume spherical symmetry, a radial decomposition of the matter distri-

---

[1] At t=0 the projectile and target surfaces are separated by approximately 2 fm.

bution predicted by the BNV model was performed [45,46]. The average binding energies of spherical shells of 1 fm thickness were estimated. Two sets of input parameters were then extracted: the first including the first "unbound" shell (R_S=9 fm), and the second including only bound shells (R_S=8 fm). The charge, mass, thermal excitation energy, and collective radial energy were used as input for the EES calculations. Only a single set of input parameters was used in the GEMINI calculations corresponding to the higher excitation energy case, R_S=9 fm. Because GEMINI does not allow expansion, the excitation energy was taken to be the sum of the thermal and radial expansion energies. A triangular angular momentum distribution between 0 and 70 $\hbar$ was used in the GEMINI calculations[2].

The BMM assumes fragment formation from a nuclear system at low density. Therefore, the coupling with the dynamical calculation was chosen to be at the point of maximum expansion (t=115 fm/c, ρ/ρ_0=0.6) [51,52]. Two calculations were performed with the BMM model: the first with a standard radius parameter of 2.1 fm (R_{FO}=11.8 fm), and the second with an extended radius parameter of 2.6 fm (R_{FO}=14.6 fm). The values of the parameters used in the statistical model calculations are listed in Table I.

IV. RESULTS AND DISCUSSION

A. Charged-particle and Fragment Multiplicities

The measured charged-particle multiplicity, N_C, distribution (Fig. 2, top), which includes particles detected but not identified, shows a broad, flat region extending to multiplicities of approximately 13 and a sharply falling tail at larger multiplicities. An approximate impact-parameter scale is given at the top of the figure [64], where b_{max} is the impact

---

[2] In the calculation, 70 $\hbar$ is the maximum angular momentum the source can sustain with a non-zero fission barrier. BNV calculations at b=4 fm (the impact parameter bounding the most central 14% of the geometric cross section (see below) give angular momenta greater than 70 $\hbar$.

parameter corresponding to the minimum-bias trigger, N_C=2. The relationship between the average detected IMF multiplicity ($3 \leq Z \leq 20$) and the measured charged particle multiplicity is shown in the bottom panel of Fig. 2. The average IMF multiplicity is strongly correlated with N_C up to charged-particle multiplicities of about 15. Beyond this value, the average IMF multiplicity saturates at a value of approximately 1.7. For the highest measured values of N_C, in this case $N_C > 15$, the charged-particle multiplicity is no longer a good indicator of impact parameter, or energy deposition [65]. In this paper, we will concentrate on the most violent events with $N_C \geq 14$, which correspond to the upper 14% of the multiplicity distribution, and to reduced impact parameters of $b/b_{max} < 0.37$.

The measured (solid points) and predicted (curves) IMF multiplicity distributions for events with $N_C \geq 14$ are shown in Fig. 3. The detector acceptance and efficiency have been taken into account in the predictions (filtered calculations). The GEMINI calculation (solid curve) underpredicts the probabilities for multiplicities $N_{IMF} > 1$ by one or more orders of magnitude. The region spanned by the two EES calculations is indicated by horizontal hatching. These two calculations bracket the data. The region spanned by the BMM calculations is indicated by the vertical hatching. These calculations overpredict multiplicities $N_{IMF} > 2$ by approximately a factor of two. EES calculations which do not allow expansion ("Evap") are indicated by the angled hatching. In these calculations, probabilities for $N_{IMF} \geq 2$ are predicted to be smaller than observed by more than a factor of two. As found in reactions at higher bombarding energy, it is necessary to allow expansion either implicitly (BMM) or explicitly (EES) in order to generate an adequate number of fragments. [41–44]. However, the difference between the calculations with and without expansion is much smaller than that observed at higher energy.

The IMF charge distribution measured in events with $N_C \geq 14$ is shown by the solid points in Fig. 4. The experimental charge distribution exhibits a steep decrease for $3 \leq Z \leq 10$ and a more gradual falloff for larger atomic numbers. Raw and filtered calculations with the BMM model and with GEMINI are depicted by the dot-dashed and solid curves, respectively.

The BMM calculations (Fig. 4, top and middle panels) give good qualitative agreement with the experimental charge distributions over the entire atomic number range of $3 \leq Z \leq 40$. Conversely, the GEMINI calculation (bottom panel) underpredicts the yields of fragments of $Z \leq 6$ by an order of magnitude and predicts a nearly flat charge distribution.

Calculations with the EES model are compared with the data in Fig. 5. This model does not allow emission of fragments heavier than $Z = 9$. The shape of the experimental charge distribution is best reproduced by the EES calculation with $R_S = 8$ fm (top panel). The calculation with $R_S = 9$ fm (bottom panel) systematically overpredicts the measured fragment yields. The greatly-overpredicted yields for $7 \leq Z \leq 9$ may be a consequence of the increased expansion which occurs in the calculation with the larger initial radius. In the EES model, there is an energy gain ("coalescence heating") associated with the emission of heavy fragments from dilute systems [60].

The magnitude of the fragment yields suggest that expansion may be important even at $E/A = 30$ MeV; or that other dynamical effects not treated in the statistical models provide enhanced fragment emission.

B. Correlation Functions

Determination of the fragment emission time scale may provide further information about the disassembly mechanism. In order to obtain a measure of this time scale we have compared the experimental two-fragment ($4 \leq Z \leq 9$) reduced-velocity correlation function [21–30]

$$1 + R(V_{red}) = C\frac{\sum Y(\mathbf{v}_1, \mathbf{v}_2)}{\sum Y(\mathbf{v}_1)Y(\mathbf{v}_2)} \tag{2}$$

with schematic, three-body trajectory calculations described in ref. [30][3]. Here $Y(\mathbf{v}_1, \mathbf{v}_2)$ is the coincidence yield of fragments with velocities $\mathbf{v}_1$ and $\mathbf{v}_2$[4], and $Y(\mathbf{v}_1)$ and $Y(\mathbf{v}_2)$ are

---

[3] The code described herein reproduces the calculations of refs. [22–25].

[4] The laboratory velocities were calculated from the measured atomic numbers and energies assuming a fragment mass of $A = 2Z$.

the singles yields of fragments with the corresponding velocities; V_{red} is the reduced relative velocity, $V_{red} = \mid \mathbf{v}_1 - \mathbf{v}_2 \mid / \sqrt{Z_1 + Z_2}$; and C is a normalization constant equal to the ratio of the total denominator events to the total numerator events [28,29]. The reduced relative velocity, V_{red}, is introduced to eliminate the charge dependence of the relative fragment velocity in mixed-fragment correlation functions [23]. The uncorrelated distribution in the denominator of the correlation function was constructed by selecting $\mathbf{v}_1$ and $\mathbf{v}_2$ values from different events ("event-mixing technique"). Only fragments detected with the high-resolution MULTICS array provided data for the correlation functions. Approximately 37% of the fragments detected in $N_C \geq 14$ events were measured with the MULTICS array.

The experimental correlation function (Fig. 6) exhibits a depletion for $V_{red} < 0.015$ c, which is sensitive to the space-time distribution of coincident fragments. The enhancement at $V_{red} = 0.018$ c has been observed previously [25,26], and has been theoretically associated with the existence of a residue much more massive than an IMF [28]. In Fig. 6, the data are compared with calculations assuming a source radius of R_S=12 fm, with various mean emission times ranging from 0 to 500 fm/c. A source charge of Z_S=77, as determined from the BNV calculations, was used in the simulations (see below), and the measured energy and angular distributions were employed in the calculations. Best agreement with the data is obtained for an emission time of τ=200 fm/c (solid curve). To quantify the level of agreement, a contour plot of the reduced chi-squared values versus τ and R_S is shown as an inset in the figure [5]. For all assumed source radii between 8 and 14 fm, a mean emission time of 200 fm/c gives the best agreement with the data. The calculated correlation functions are sensitive to the assumed radius parameter for emission time scales < 100 fm/c; for longer time scales, the calculations become insensitive to R_S. The measured time scale of 200 fm/c

---

[5] The chi-squared values were determined over the rising portion of the correlation function, 0.004 c $\leq V_{red} \leq$ 0.017 c. At larger reduced velocity, the correlation function is less sensitive to the space-time distribution of fragments, and more sensitive to effects such as the charge of the emitting source [28] (see Fig. 7 below). An investigation of these effects is beyond the scope of this paper.

is consistent with that of sequential decay. We note that a ^{12}C fragment with a kinetic energy of 13 MeV (approximately twice the predicted temperature of the ^{129}Xe + ^{nat}Cu system in a central collision) will travel a distance corresponding to 1.75 times its diameter in a time of 200 fm/c.

In the three-body trajectory calculations, the initial energy of the emitted fragments, prior to Coulomb acceleration, is

$$E_{init} = \frac{m}{2} \mid \mathbf{v}_{lab} - \mathbf{v}_S \mid^2 - E_{coul}, \tag{3}$$

where m is the fragment mass, $\mathbf{v}_{lab}$ is the measured fragment velocity vector determined by a Monte Carlo sampling of the experimental energy and angular distributions, $\mathbf{v}_S$ is the assumed source velocity vector, and E_{coul} is an estimated Coulomb repulsion energy calculated from the source radius, R_S, and source charge, Z_S, as

$$E_{coul} = \frac{1.44 Z_S Z_{frag}}{R_S + R_{frag}}. \tag{4}$$

The fragment radius, R_{frag}, is taken to be $1.2A_{frag}^{1/3}$. This simple two-sphere parameterization of the decay configuration neglects thermal shape fluctuations at the scission point [59,67] and polarization of the charge during the decay process, which could decrease the emission energy as in the case of low-energy binary fission [68].

For some fraction of the experimental energy spectra, the calculated value of E_{init} is < 0 ("sub-barrier emission"). In the three-body trajectory code these events are discarded and the measured energy spectra are sampled again. The percentage of the experimental energy spectra that is sampled depends upon the values of the parameters Z_S and R_S. The correlation functions with R_S = 12 and 14 fm, and Z_S = 25, 40, 50 and 77 are shown in Fig. 7. The bump near V_{red} = 0.020 c disappears for smaller values of Z_S, as demonstrated by Schapiro et al. [28], but the rising portions of the correlation functions are very similiar for all calculations with $Z_S > 25$. For R_S= 12 fm, a choice of Z_S = 50 provides the best agreement with the data, while for R_S= 14 fm, the calculations for Z_S = 50 and 77 are indistinguishable. In contrast, the sampled fractions of the energy distribution are very sensitive to the value of Z_S. These fractions range from 0.4 to 0.90 for $Z_S = 77$ to 40. This demonstrates that the time scales extracted from the trajectory calculations are not very dependent on the initial energy distribution.

Alternatively, one may set a threshold on the experimental energy spectra and study correlations between fragments with emission energies "above the barrier" [30]. In reverse kinematics reactions, where the source moves with a large velocity, it is necessary to transform into the source frame before setting a energy threshold. The correlation function for fragments with energies of $E/A > 2.5$ MeV in the source frame (see below) is shown as the open points in Fig. 8 [6]. These events with two or more high-energy fragments correspond to $\approx$ 13% of all events with two or more fragments detected with the MULTICS array. The curves in the figure depict calculations with the three-body trajectory code for a source charge of 50, a source radius of 12 fm, and mean emission times of 200 (solid), 100 (dashed), and 0 (dotted) fm/c after applying the same energy threshold. Approximately 43% of the simulated events pass through this energy filter. Comparison of the gated correlation function with the simulations indicates a faster emission time scale $0 \leq \tau \leq 100$ fm/c for these higher-energy fragments. These fragments can be understood as originating early in the decay chain from systems with higher temperature and more charge (hence, increased Coulomb emission energy). Previous work has also indicated a smaller emission time for fragments of higher energy [22,30].

The fragment emission time scale of $\approx$ 200 fm/c determined from the trajectory calculations can be directly compared with the mean emission time calculated with the EES model. Mean emission times of ~190 fm/c and ~110 fm/c were calculated for the two cases with initial radii of 8 fm, and 9 fm, respectively. The mean emission time for the R_S=8 fm case, determined solely from the input parameters provided by the BNV calculations,

---

[6] A laboratory frame threshold of $E/A > 6$ MeV was employed in ref. [30]. At a laboratory angle of 20°, this threshold corresponds to $E/A = 2.2$ MeV in the center-of-mass frame, and is therefore similiar to what was used in the present work.

agrees quantitatively with the experimental emission time determined from the trajectory calculations.

In Fig. 9 the experimental correlation function is compared with calculations generated by the three statistical decay models. For the GEMINI and BMM calculations the simulated-event files were filtered through a software replica of the MULTICS array. For the EES calculations the three-body trajectory code described above was modified to generate correlation functions based on the theoretical charge distributions, emission time distributions, and the (time-dependent) source charge, mass, temperature and radius. These calculated events were then passed through the experimental filter. In the top panel, correlation functions based upon the R_S=8 fm (dashed curve) and R_S=9 fm (dotted curve) EES calculations are shown. Although the calculated emission times agree well with those determined from the trajectory calculations, the correlation functions exhibit differences. Because the angular distributions assumed in the EES model do not correspond to the experimental angular distributions (see below), the initial positioning of the fragments in the EES and trajectory calculations differs. This difference in initial conditions has a discernable effect on the calculated correlation functions.

The direction of the initial radius vector of each fragment was chosen according to Lambert's law for surface emission, $P(\theta) \propto \cos\theta$, where θ is the angle between the radius vector and the previously-determined velocity vector. Hence, different angular distributions of the fragments result in different initial spatial distributions.

Replacing the isotropic angular distributions assumed by the EES model with the experimental angular distributions leads to the correlation functions shown in Fig. 9 by the solid (R_S=8 fm) and dot-dashed (R_S=9 fm) curves. The agreement of these calculations with the data is much improved, demonstrating that realistic single-particle distributions must be used for quantitative analyses of correlation functions.

The bottom panel of Fig. 9 shows the correlation functions predicted by GEMINI and the BMM model. The GEMINI calculation (dotted curve), which assumes an infinite time between emissions, gives an incorrect shape. Approximately one-half of the coincident fragment-fragment pairs predicted by GEMINI are formed by the binary splitting of a primary parent. This process gives rise to a well-defined relative velocity between the two IMFs and a strong peak in the correlation function that is not observed in the data.

The BMM calculation with the standard radius of 11.8 fm (dashed curve) also gives poor agreement with the data. Better agreement is obtained (solid curve) with a larger radius of R_S = 14.6 fm, as observed for peripheral collisions at E/A = 50 MeV [29]. However, because of the dual sensitivity of the correlation function to space and time, such a large radius may be unrealistic and mimic a finite lifetime that is not considered in the BMM model. To determine if simultaneous fragment emission from a greatly-expanded system is realistic, we examine the fragment emission patterns predicted by the different decay models in the following section.

C. Velocity and Angular Distributions

A widely-used technique for isolating the sources contributing to fragment emission is to plot the cross section in velocity space for a given atomic number as $d^2\sigma/dv_{\|}dv_{\perp}$ [25,34–36,49,50]. This is a particularly powerful technique when a global observable such as the charged-particle multiplicity or the total detected charge is used as an event selector. For example, in the ^{139}La + ^{nat}Ni reaction at E/A = 18 MeV [34] the total detected charge was used to select a range of momentum/mass transfers in the incomplete fusion process, and to demonstrate the simple, binary nature of the decay; in the ^{129}Xe+ ^{nat}Cu reaction at E/A = 50 MeV, multiplicity-gated velocity distributions were used to demonstrate the evolution of the reaction mechanism from the sequential decay of projectile- and target-like fragments in peripheral reactions to the fast disassembly of a single anisotropic "source" in central collisions [25].

We now examine the distribution of C fragments in velocity space in order to determine the degree of relaxation of the kinetic energy and angular degrees of freedom. Statistical models stipulate that the angular distributions of the fragments be forward/backward symmetric in the frame of the decaying system. The predicted emission velocities are determined primarily by the Coulomb repulsion energy between the emitted fragment and the residual system, and are independent of emission angle.

In the upper left-hand panel of Fig. 10 the experimental distribution of C fragments in velocity space is shown for events with $N_C \geq 14$. The discontinuities in the distribution are caused by detector acceptance effects; for laboratory angles > 23° the events have been randomized over the face of the struck Miniball detector. There is a depletion of events centered approximately at $v_{\|} = 0.17$ c, $v_{\perp} = 0$ c, which corresponds nearly to the center-of-mass velocity of the system (arrow). Such a "Coulomb hole" is a signature of binary decay of a system with a sharply-defined velocity and a significant charge, and is consistent with a statistical emission process. The distribution of events around the Coulomb hole, however, is not isotropic. There are more events at backward angles in the frame of the decaying system than at forward angles.

In order to characterize the emission patterns more quantitatively, we have employed the coincident-fragment source-velocity technique developed in ref. [34] to determine the average velocity of the decaying system. A detected charge of $Z_{total} > 35$ was required to exclude events in which only a small fraction of the momentum was measured. The source velocity distributions are shown in Fig. 11 for 3-fold, 4-fold, and 5-fold fragment ($Z > 2$) events. The mean and standard deviation of the integrated distribution were determined to be 0.174 c and 0.015 c, respectively. This average source velocity corresponds to nearly full (92%) momentum transfer in the simple incomplete fusion model.

The distributions of C fragments in velocity space predicted by the statistical decay models are shown in Fig. 10 [panels (b), (c), and (d)] after boosting by the average source velocity and filtering through the experimental acceptance. As required by the statistical emission hypothesis, the calculated velocity distributions exhibit well-defined Coulomb holes and Coulomb circles, and forward/backward symmetric angular distribution which are not observed in the data. The radii of the predicted circles depends mainly upon the Coulomb energy of the decay configuration, which in turn depends upon the assumed break-up geometry in each of the models (see below).

The experimental data were transformed event-by-event into the average source frame determined from the source velocity distribution. The solid points in Fig. 12 (top) depict the angular distribution of C fragments in this frame as a differential multiplicity, namely fragments per event per radian. The yield rises slowly with angle beyond 30° and reaches a pronounced maximum near 150°. Assuming that all of the fragments emitted forward of 90 degrees arise from fully relaxed statistical emission, the forward/backward ratio of the differential cross section can be used to estimate the degree of equilibration of the angular degrees of freedom [36]. Such a decomposition for angles of $30^\circ - 150^\circ$ gives an equilibrium fraction of $\approx$78% for $N_C \geq 14$ events. The open points in the top panel of Fig. 12 depict the experimental angular distribution for events with $N_C \geq 19$, which corresponds to $\sim$0.4% of the total number of events with $N_C > 2$. The equilibrium fraction of C fragments in these events is $\approx$85%. Thus, gating on the extreme tail of the charged-particle multiplicity distribution selects a more equilibrated set of events, however, complete relaxation of the angular degrees of freedom is still not observed.

The angular distribution of C fragments predicted by the EES model with $R_S = 8$ fm is indicated by the dot-dashed curve in the top panel of Fig. 12. This angular distribution is isotropic ($dP/d\Omega =$ constant, $dP/d\theta \propto \sin\theta$) in the source frame and is similiar in shape to those predicted by the other statistical models, except at very small and very large angles where detector acceptance effects are encountered. The agreement of the predicted angular distributions with the data is excellent for emission angles $< 90^\circ$ (there is no normalization factor between theory and data), but the backward-peaking observed in the experimental distribution is inconsistent with equilibrium statistical decay from a single source, which requires forward/backward symmetric decay patterns.

The mean emission velocities of C fragments are shown in Fig. 12 (bottom) as a function of emission angle in the source frame. The nearly constant values of V_{Emiss} over the range of θ_S=35°-115° are consistent with equilibrium emission. The larger values of V_{Emiss} at small θ_S are caused by the experimental acceptance (note the similiarity of the data and the statistical model calculations described below). The increase at larger θ_S is indicative of the additional component of fragment emission which was apparent in the source-frame angular distributions.

The enhancement in the differential cross section at backward angles, > 100 °, signifies the existence of fragments with either a target-like or a neck origin [69,70]. The mean emission velocities of these fragments are too large to be explained by equilibrium emission from a fusion-like source.

After boosting by the average source velocity and filtering through the response of the experimental apparatus, the calculated mean emission velocities of C fragments are presented in the bottom panel of Fig. 12. The two EES calculations ($R_S = 8$ fm shown) overpredict the average emission velocity in the θ_S range where equilibrium emission dominates. An EES calculation that does not allow expansion ("Evap") overpredicts the data even more greatly. The GEMINI calculation shows good agreement with the data, whereas the BMM calculation with a radius of 11.8 fm underpredicts, and that with a radius of 14.6 fm greatly underpredicts the average emission velocities.

The predicted emission velocities are smaller for the BMM calculations with the larger radius because of the decreased Coulomb energy of the expanded decay configuration. There is a trade-off in the BMM calculations between providing good agreement with the fragment-fragment correlation functions (larger radius) or providing better agreement with the fragment emission velocities (smaller radius). The lack of a concerted good agreement indicates that simultaneous decay as assumed by the BMM model is an unlikely scenario. The mechanism is apparently characterized by an effective radius smaller than 14.6 fm, and by a finite lifetime.

In the EES model, the emission energy consists of Coulomb, thermal, and collective components. The Coulomb energy is calculated by a simple two-sphere parameterization for binary decay. The Coulomb component is

$$E_{Coul} = \frac{e^2 Z_{res} Z_{frag}}{1.2(R_{res} + R_{frag})}, \quad (5)$$

where Z_{frag} and Z_{res} are the atomic numbers of the emitted fragment and the residual nucleus, respectively; R_{res} is the (time-dependent) radius of the emitting source; and R_{frag} is the radius of the emitted fragment ($= 1.2A_{frag}^{1/3}$). The thermal contribution to the emission energy follows a Maxwell distribution, $P(E_{therm}) \propto E_{therm}e^{-E_{therm}/T}$. The collective component results from the expansion or contraction of the source. For fragment emission, the bulk of the emission energy is contained in the Coulomb component.

An EES calculation which does not allow expansion ("Evap") predicts larger emission velocities because of the increased Coulomb energy in the more compact decay configuration. The collective radial velocity of expansion in the standard EES calculations is not enough to offset the increase in Coulomb energy. The EES calculations with R_S=9 fm predict slightly smaller Coulomb energies and slightly larger radial energies than those with R_S=8 fm because of the greater expansion of the source. However, the calculated emission velocities are nearly identical for the two initial source radii.

In GEMINI the emission energy consists of Coulomb and rotational components. The Coulomb component is

$$E_{Coul} = \frac{1.44 Z_{frag} Z_{res}}{1.16(A_{frag}^{1/3} + A_{res}^{1/3}) + 2}, \tag{6}$$

where Z_{frag}, Z_{res}, and A_{frag} are defined as above, and A_{res} is the mass number of the residual nucleus. The rotational component depends upon the orbital angular momentum of emission, J, and contributes little to the total emission energy. GEMINI also allows for sequential decay of the excited primary fragments which leads to a reduction in the average emission velocity for a given atomic number.

The better agreement predicted by GEMINI appears to result from the empirical radius parameterization (2 fm separation between partners), which reproduces the low-energy binary-decay systematics [33,36]. This parameterization may mimic the shape polarization effects mentioned above which decrease the average Coulomb energies. A realistic treatment of such polarization effects requires a dynamical description of fragment emission [71–75]. A reduction of the Coulomb barrier in the EES model by 10% for the R_S = 8 fm calculation also provides improved agreement with the measured IMF multiplicity distribution (Fig. 3) and the mean C emission velocity (Fig. 12), with only a slight decrease in the predicted emission times ($\tau = 180$ fm/c).

V. SUMMARY

We have studied central ($N_C \geq 14$) collisions of ^{129}Xe with ^{nat}Cu. The experimental data has been compared with three statistical models with input based upon a dynamical BNV code. Standard values of the parameters in each model were employed with no attempt to adjust them to optimize the agreement with the data. Calculations with the binary decay model GEMINI drastically underpredict the fragment multiplicity. In contrast, the models which allow expansion either explicitly (EES) or implicitly (BMM) are able to generate an adequate number of fragments. This result suggests that expansion or other dynamical effects may be important for the production of fragments in this reaction.

The EES model predicts an approximately correct mean fragment emission time, as determined by the trajectory calculations, but the correlation function is not well reproduced. Use of the experimental angular distributions improves the agreement with the experimental correlation functions. This illustrates the need for models to reproduce single-particle observables as well as more complex quantities.

The multi-particle phase space BMM model gives good agreement with the experimental charge distribution. Varying the radius parameter in this model can provide good agreement with the fragment-fragment correlation function (large radius simulating a finite lifetime) or improved agreement with the fragment emission velocities (standard radius), but not with both simultaneously. This result corroborates the analysis of the fragment-fragment reduced-velocity correlations with three-body trajectory calculations, which indicates a mean fragment emission time of ≈200 fm/c, and signifies a sequential emission time scale.

The experimental angular distributions and the emission velocities of C fragments were found to be inconsistent with fully-equilibrated statistical emission from a single source.

The mean emission velocities of C fragments show best agreement with the predictions of GEMINI, probably because this model takes an empirical parameterization of the decay radius based upon low-energy systematics. An extended radius parameter may mimic shape polarization effects which lead to the low fragment velocities observed in low-energy fission. In order to for allow such polarization effects and to provide for non-equilibrium emission mechanisms, dynamical models of fragment formation are required. [71–75].

This work was supported by the National Science Foundation under Grants PHY-90-15255 and PHY-92-14992.

REFERENCES

[1] C.B. Chitwood, D.J. Fields, C.K. Gelbke, W.G. Lynch, A.D. Panagiotou, M.B. Tsang, H. Utsunomiya, and W.A. Friedman, Phys. Lett. B **131**, 289 (1983).

[2] D.J. Fields, W.G. Lynch, C.B. Chitwood, C.K. Gelbke, M.B. Tsang, H. Utsunomiya, and J. Aichelin, Phys. Rev. C **30**, 1912 (1984).

[3] W. Mittig, A. Cunsolo, A. Foti, J.P. Wieleczko, F. Auger, B. Berthier, J.M. Pascaud, J. Quebert, and E. Plagnol, Phys. Lett. B **154**, 259 (1985).

[4] R. Bougault, D. Horn, C.B. Chitwood, D.J. Fields, C.K. Gelbke, D.R. Klesch, W.G. Lynch, M.B. Tsang, and K. Kwiatkowski, Phys. Rev. C **36**, 830 (1987).

[5] F. Auger, B. Berthier, A. Cunsolo, A. Foti, W. Mittig, J.M. Pascaud, E. Plagnol, J. Quebert, and J.P. Wieleczko, Phys. Rev. C **35**, 190 (1987).

[6] M. Fatyga et al., Phys. Rev. Lett. **58**, 2527 (1987).

[7] B. Borderie, M. Montoya, M.F. Rivet, D. Jouan, C. Cabot, H. Fuchs, D. Gardes, H. Gauvin, D. Jacquet, and F. Monnet, Phys. Lett. B **205**, 26 (1988)

[8] M.F. Rivet, B. Borderie, C. Gregoire, D. Jouan, and B. Remaud, Phys. Lett. B **215**, 55 (1988).

[9] R. Trockel et al., Phys. Rev. C **39**, 729 (1989).

[10] Y.D. Kim et al., Phys. Rev. Lett. **63**, 494 (1989).

[11] T. Ethvignot et al., Phys. Rev. C **43**, R2035 (1991).

[12] Y. Blumenfeld et al., Phys. Rev. Lett. **66**, 576 (1991).

[13] E. Piasecki et al., Phys. Rev. Lett. **66**, 1291 (1991).

[14] B. Lott et al., Phys. Rev. Lett. **68**, 3141 (1992).

[15] M. Louvel et al., Nucl. Phys. **A559**, 137 (1993).

[16] J.F. Lecolley et al., Phys. Lett B **325**, 317 (1994).

[17] D. Horn, G.C. Ball, D.R. Bowman, A. Galindo-Uribarri, E. Hagberg, R.B. Walker, R. Laforest, and J. Pouliot, Proceedings of the Workshop on Heavy-Ion Fusion, Padua, Italy, May 25-27, 1994.

[18] R. Bougault, J. Colin, F. Delaunay, A. Genoux-Lubain, A. Hajfani, C. Le Brun, J.F. Lecolley, M. Louvel, and J.C. Steckmeyer, Phys. Lett. B **232**, 291 (1989).

[19] R. Trockel et al., Phys. Rev. Lett. **59**, 2844 (1987).

[20] V. Lips et al., Phys. Lett. B **338**, 141 (1994).

[21] B. Kämpfer et al., Phys. Rev. C **48**, R955 (1993).

[22] Y.D. Kim, R.T. de Souza, D.R. Bowman, N. Carlin, C.K. Gelbke, W.G. Gong, W.G. Lynch, L. Phair, M.B. Tsang, and F. Zhu, Phys. Rev. Lett. **67**, 14 (1991); Phys. Rev. C **45**, 338 (1992).

[23] Y.D. Kim, R.T. de Souza, C.K. Gelbke, W.G. Gong, and S. Pratt, Phys. Rev. C **45**, 387 (1992).

[24] D. Fox et al., Phys. Rev. C **47**, R421 (1993); C **48**, 3135(E) (1993).

[25] D.R. Bowman et al., Phys. Rev. Lett. **70**, 3534 (1993).

[26] T.C. Sangster, M. Begemann-Blaich, T. Blaich, H.C. Britt, A. Elmaani, N.N. Ajitanand, and M.N. Namboodiri, Phys. Rev. C **47**, R2457 (1993).

[27] E. Bauge et al., Phys. Rev. Lett. **70**, 3705 (1993).

[28] O. Schapiro, A.R. DeAngelis, and D.H.E. Gross, Nucl. Phys. **A568**, 333 (1994).

[29] O. Schapiro and D.H.E. Gross, Nucl. Phys. **A573**, 143 (1994).

[30] T. Glasmacher et al., Phys. Rev. C **50**, 952 (1994).

[31] O. Lopez et al., Phys. Lett. B **315**, 34 (1993).

[32] M. Louvel et al., Phys. Lett B **320**, 221 (1994).

[33] L.G. Sobotka, M.A. McMahan, R.J. McDonald, C. Signarbieux, G.J. Wozniak, M.L. Padgett, J.H. Gu, Z.H. Liu, Z.Q. Yao, and L.G. Moretto, Phys. Rev. Lett. **53**, 2004 (1984).

[34] N. Colonna et al., Phys. Rev. Lett. **62**, 1833 (1989).

[35] R.J. Charity et al., Nucl. Phys. **A483**, 371 (1988).

[36] R.J. Charity, D.R. Bowman, Z.H. Liu, R.J. McDonald, M.A. McMahan, G.J. Wozniak, L.G. Moretto, S. Bradley, W.L. Kehoe, and A.C. Mignerey, Nucl. Phys. **A476**, 516 (1988).

[37] D.E. Fields et al., Phys. Lett. B **220**, 356 (1989).

[38] J.L. Wile et al., Phys. Rev. C **45**, 2300 (1992).

[39] R.T. de Souza et al., Phys. Lett. B **300**, 29 (1993).

[40] K. Kwiatkowski, W.A. Friedman, L.W. Woo, V.E. Viola, E.C. Pollacco, C. Volant, and S.J. Yennello, Phys. Rev. C **49**, 1516 (1994).

[41] D.R. Bowman et al., Phys. Rev. Lett. **67**, 1527 (1991).

[42] R.T. de Souza et al., Phys. Lett. B **268**, 6 (1991).

[43] K. Hagel et al., Phys. Rev. Lett. **68**, 2141 (1992).

[44] J. Hubele et al., Phys. Rev. C **46**, R1577 (1992).

[45] D.R. Bowman et al., Phys. Rev. C **46**, 1834 (1992).

[46] W.J. Llope et al., National Superconducting Cyclotron Laboratory preprint MSUCL-908

[47] S.C. Jeong et al., Phys. Rev. Lett. **72**, 3468 (1994).

[48] W.C. Hsi et al., MSU preprint, MSUCL-930 (1994).

[49] K. Hanold, L.G. Moretto, G.F. Peaslee, G.J. Wozniak, D.R. Bowman, M.F. Mohar, D.J. Morrissey, Phys. Rev. C **48**, 723 (1993).

[50] P. Roussel-Chomaz et al., Nucl. Phys. **A551**, 508 (1993).

[51] M. Colonna, P. Roussel-Chomaz, N. Colonna, M. Di Toro, L.G. Moretto, and G.J. Wozniak, Phys. Lett B **283**, 180 (1992).

[52] M. Colonna, N. Colonna, A. Bonasera, and M. Di Toro, Nucl. Phys. **A541**, 295 (1992).

[53] I. Iori et al., Nucl. Instr. Meth. A **325**, 458 (1993).

[54] R.T. de Souza et al., Nucl. Instr. Meth. A **295**, 109 (1990).

[55] M.A. McMahan, G.J. Wozniak, C.M. Lyneis, D.R. Bowman, R.J. Charity, Z.H. Liu, L.G. Moretto, W.L. Kehoe, A.C. Mignerey, and M.N. Namboodiri, Nucl. Instr. Meth. A **253**, 1 (1986).

[56] N. Colonna and E. Lisi, Nucl. Instr. Meth. A **334**, 551 (1994).

[57] C. Schwarz, W.C. Hsi, M.J. Huang, D.R. Bowman, Y.D. Kim, W.G. Lynch, L. Phair, and M.B. Tsang, National Superconducting Cyclotron Laboratory Annual Report, 248 (1993).

[58] H. Hauser and H. Feshbach, Phys. Rev. **87**, 366 (1952).

[59] L.G. Moretto Phys. Lett. B **40**, 185 (1972); Nucl. Phys. **A247**, 211 (1975).

[60] W.A. Friedman, Phys. Rev. Lett. **60**, 2125 (1988).

[61] D.H.E. Gross, Rep. Prog. Phys. **53**, 605 (1990).

[62] B. Lott et al., Z. Phys. A **346**, 201 (1993).

[63] A. Bonasera et al., Phys. Lett. B **221**, 233 (1989).

[64] C. Cavata, M. Demoulins, J. Gosset, M.C. Lemaire, D. L'Hote, J. Poitou, and O. Valette, Phys. Rev. C **42**, 1760 (1990).

[65] A. Del Zoppo et al., Phys. Rev. C **49**, 3334 (1994).

[66] D.H.E. Gross, Zhang Xiao-ze, and Xu Shu-yan, Phys. Rev. Lett. **56**, 1544 (1986).

[67] L.G. Moretto and D.R. Bowman, Proceedings of the XXV International Winter Meeting on Nuclear Physics, Bormio, Italy, ed. I. Iori [Ricerca Scientifica ed Educazione Permanente, Suppl. 91 (1987)].

[68] V.E. Viola, Jr., K. Kwiatkowski, and M. Walker, Phys. Rev. C **31**, 1550 (1985).

[69] L.G. Sobotka, Phys. Rev. C **50**, R1272 (1994).

[70] C.P. Montoya et al., Phys. Rev. Lett. in press, and National Superconducting Cyclotron Laboratory preprint MSUCL-938.

[71] J. Aichelin, G. Peilert, A. Bohnet, A. Rosenhauer, H. Stöcker, and W. Greiner, Phys. Rev. C **37**, 2451 (1988).

[72] D.H. Boal and J.N. Glosli, Phys. Rev. C **38**, 1870 (1988); **38**, 2621 (1988).

[73] G. Peilert, H. Stöcker, W. Greiner, A. Rosenhauer, A. Bohnet, and J. Aichelin, Phys. Rev. C **39**, 1402 (1989).

[74] H. Feldmeier Nucl. Phys. **A515**, 147 (1990).

[75] G.F. Burgio, Ph. Chomaz, and J. Randrup, Nucl. Phys. **A529**, 157 (1991).

FIGURES

FIG. 1. BNV predictions for b=0 fm ^{129}Xe + ^{nat}Cu collisions with a compressibility parameter, K = 200 MeV. The predicted mass loss (top panel), density of the residue (second panel), excitation energy per nucleon in the residue (third panel), and collective radial energy per nucleon in the residue (bottom panel) are shown as a function of time.

FIG. 2. Top: Detected charged-particle multiplicity distribution. An approximate geometrical impact-parameter scale is given at the top of the figure. The arrow indicates the region to which the theoretical calculations were compared. Bottom: Relationship between the detected charged-particle multiplicity and the detected IMF ($3 \geq Z \geq 20$) multiplicity.

FIG. 3. Probability distribution for the detected intermediate-mass-fragment multiplicity in $N_C \geq 14$ events. The solid points indicate the measured data. The solid line corresponds to GEMINI predictions. The vertically hatched, horizontally hatched, and cross hatched regions correspond to BMM, EES (with expansion), and EES (without expansion) calculations, respectively.

FIG. 4. Experimental charge distribution (solid points) in $N_C \geq 14$ events compared with unfiltered (dot-dashed curves) and filtered (solid curves) predictions by the BMM model with a freeze-out radius of R_{FO} = 14.6 fm (top panel), the BMM model with a freeze-out radius of R_{FO} = 11.8 fm (central panel), and GEMINI (bottom panel).

FIG. 5. Experimental charge distribution (solid points) in $N_C \geq 14$ events compared with unfiltered (dot-dashed curves) and filtered (solid curves) predictions by the EES model with an initial source radius of R_S = 8 fm (top panel), and the EES model with an initial source radius of R_S = 9 fm (bottom panel).

FIG. 6. Comparison of experimental ($N_C \geq 14$) fragment-fragment reduced-velocity correlation functions (solid points) with three-body trajectory calculations (curves). The calculations were performed assuming a source radius, R_S, of 12 fm and the indicated mean emission times, τ. Inset: Contours of chi-squared per degree of freedom for three-body trajectory calculations in $\tau - R_S$ space. Solid contours correspond to levels of 10, 40, and 160. Dotted contours correpsond to levels of 20 and 80.

FIG. 7. Correlation functions predicted by three-body trajectory calculations with source charges of Z_S = 77, 50, 40, and 25 and source radii of R_S = 12 fm (top) and R_S = 14 fm (bottom) for a mean fragment emission time of 200 fm/c.

FIG. 8. Fragment-fragment reduced-velocity correlation functions in $N_C \geq 14$ events for all fragments of $4 \geq Z \geq 9$ (solid points), and for fragments of $4 \geq Z \geq 9$ with energies $E/A > 2.5$ MeV in the average source frame (open points). The curves correspond to three-body trajectory calculations with a source radius of R_S = 12 fm and mean emission times of 200 (solid), 100 (dashed), and 0 (dotted) fm/c for fragments with energies greater than 2.5 MeV.

FIG. 9. Comparison of experimental ($N_C \geq 14$) fragment-fragment reduced-velocity correlation functions (solid points) with filtered statistical model calculations. Top: EES with R_S=8 fm and experimental angular distribution (solid curve), R_S=9 fm and experimental angular distribution (dot-dashed curve), R_S=8 fm and isotropic angular distributions (dashed curve), and R_S=9 fm and isotropic angular distributions (dotted curve). Bottom: BMM with R_{FO}=14.6 fm (solid curve), BMM with R_{FO}=11.8 fm (dashed curve), and GEMINI (dotted curve).

FIG. 10. Linear density plots of the cross section in velocity space $d^2\sigma/dv_{||}dv_{\perp}$ for $Z = 6$ emission in $N_C \geq 14$ events. Upper left: experimental data, upper right: BMM model, lower left: GEMINI, lower right: EES model. The approximate low-energy threshold is depicted by the dashed lines. The center-of-mass velocity is indicated by the arrows.

FIG. 11. Source velocity distributions for the indicated number of Z $\geq$ 3 fragments in $N_C \geq$ 14 events with a total detected charge of $Z_{total} > 35$.

FIG. 12. Top: angular distributions in the source frame for $N_C \geq 14$ (solid points) and $N_C \geq 19$ events (open points). The curve corresponds to a prediction by EES model with R_S=9 fm. Bottom: The average (solid points) emission velocities in the source frame (V_S=0.174 c) as a function of emission angle in $N_C \geq 14$ events. The curves correspond to filtered calculations with the indicated statistical models.

TABLES

TABLE I. Parameters for statistical models calculations: time of the coupling, source (freeze-out) radius, charge, mass, excitation energy, and energy of radial expansion; and the mean fragment multiplicities calculated with each model.

	τ (fm/c)	r (fm)	Z	A	E^* (MeV)	E_R (MeV)	$< N_{IMF} >$
GEMINI	80	9	77	175	860	-	0.4
EES	80	9	77	175	700	160	2.0 (0.9)
EES	80	8	73	165	540	130	1.1 (0.7)
BMM	115	14.6	76	177	750	-	2.4
BMM	115	11.8	76	177	750	-	2.3

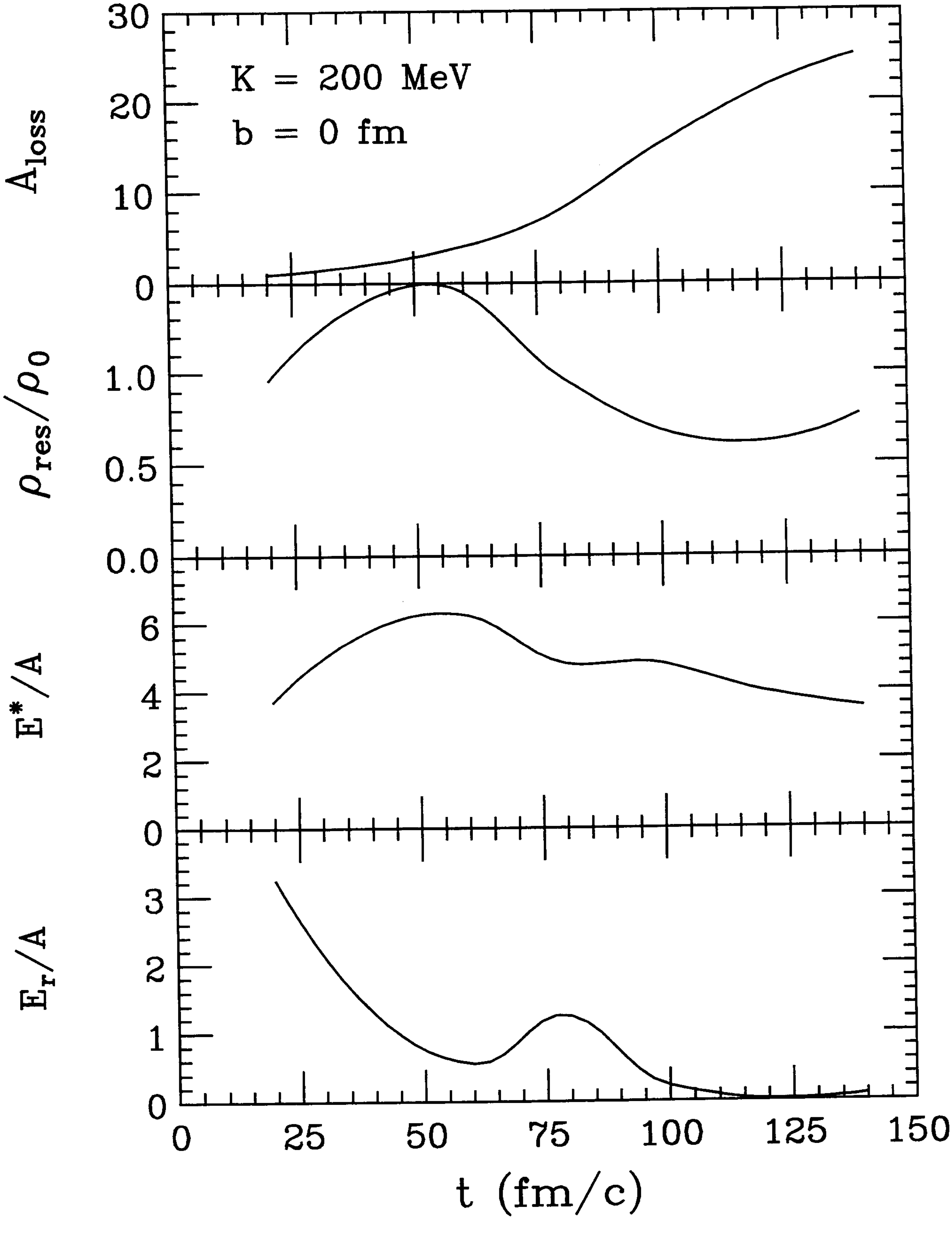
K = 200 MeV
b = 0 fm
A_{loss}
30
20
10
0
ρ_{res}/ρ_0
1.0
0.5
0.0
E^*/A
6
4
2
0
E_r/A
3
2
1
0
0
25
50
75
100
125
150
t (fm/c)

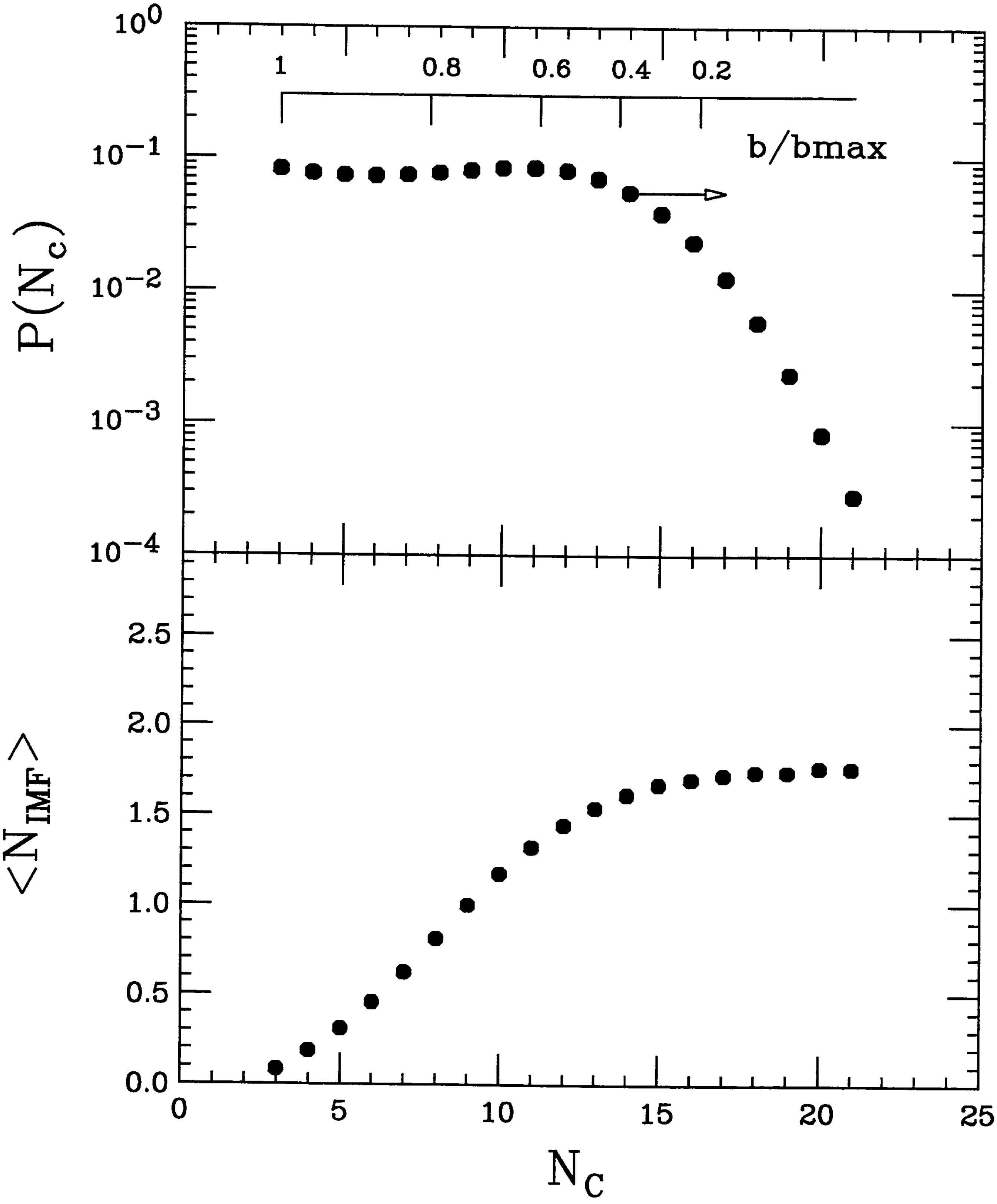

10^0
10^{-1}
10^{-2}
10^{-3}
10^{-4}
$P(N_c)$
1
0.8
0.6
0.4
0.2
b/bmax
2.5
2.0
1.5
1.0
0.5
0.0
$\langle N_{IMF} \rangle$
0
5
10
15
20
25
N_C

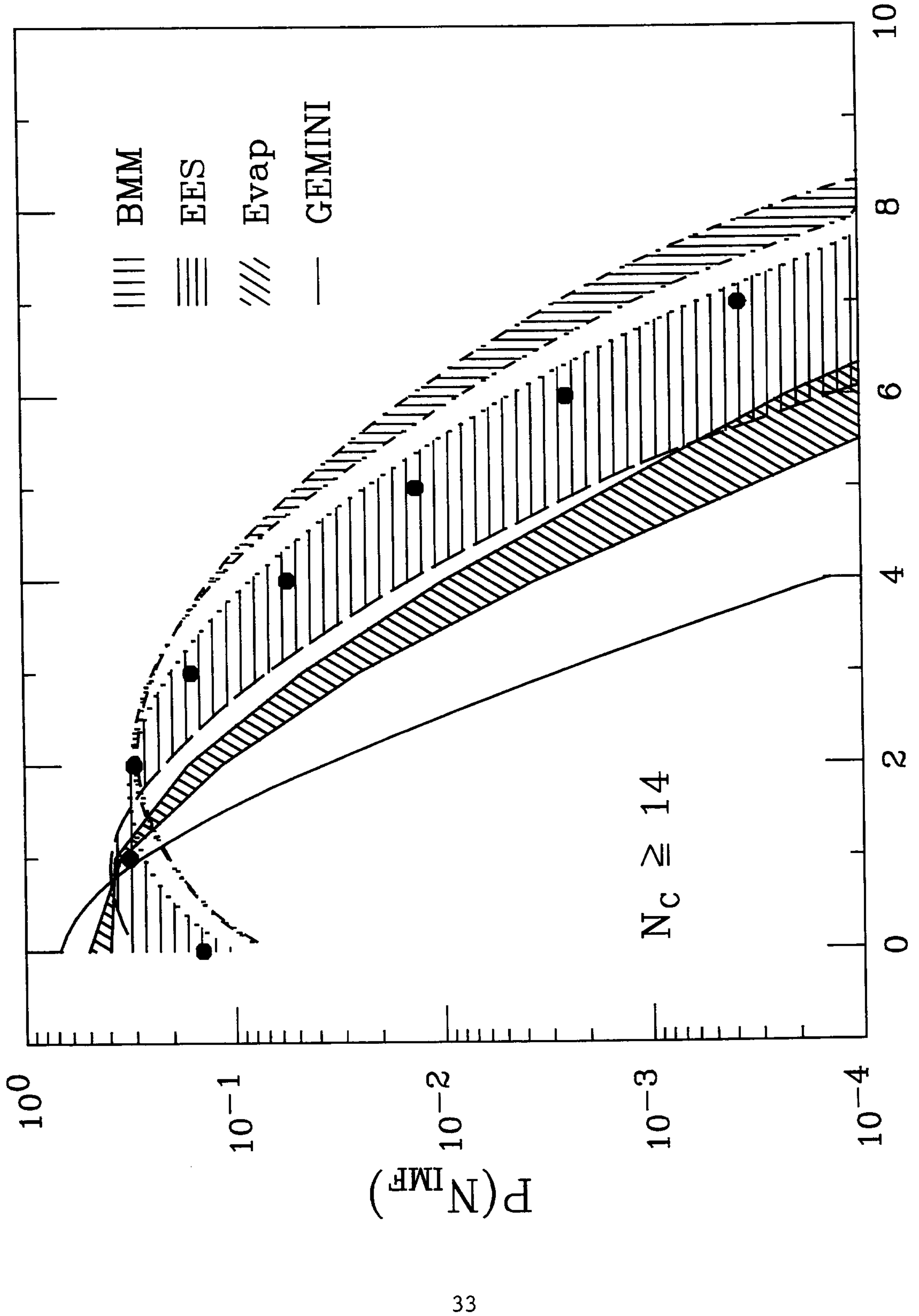
P(N_IMF)
10^0
10^-1
10^-2
10^-3
10^-4
N_IMF
0
2
4
6
8
10
N_c ≥ 14
BMM
EES
Evap
GEMINI

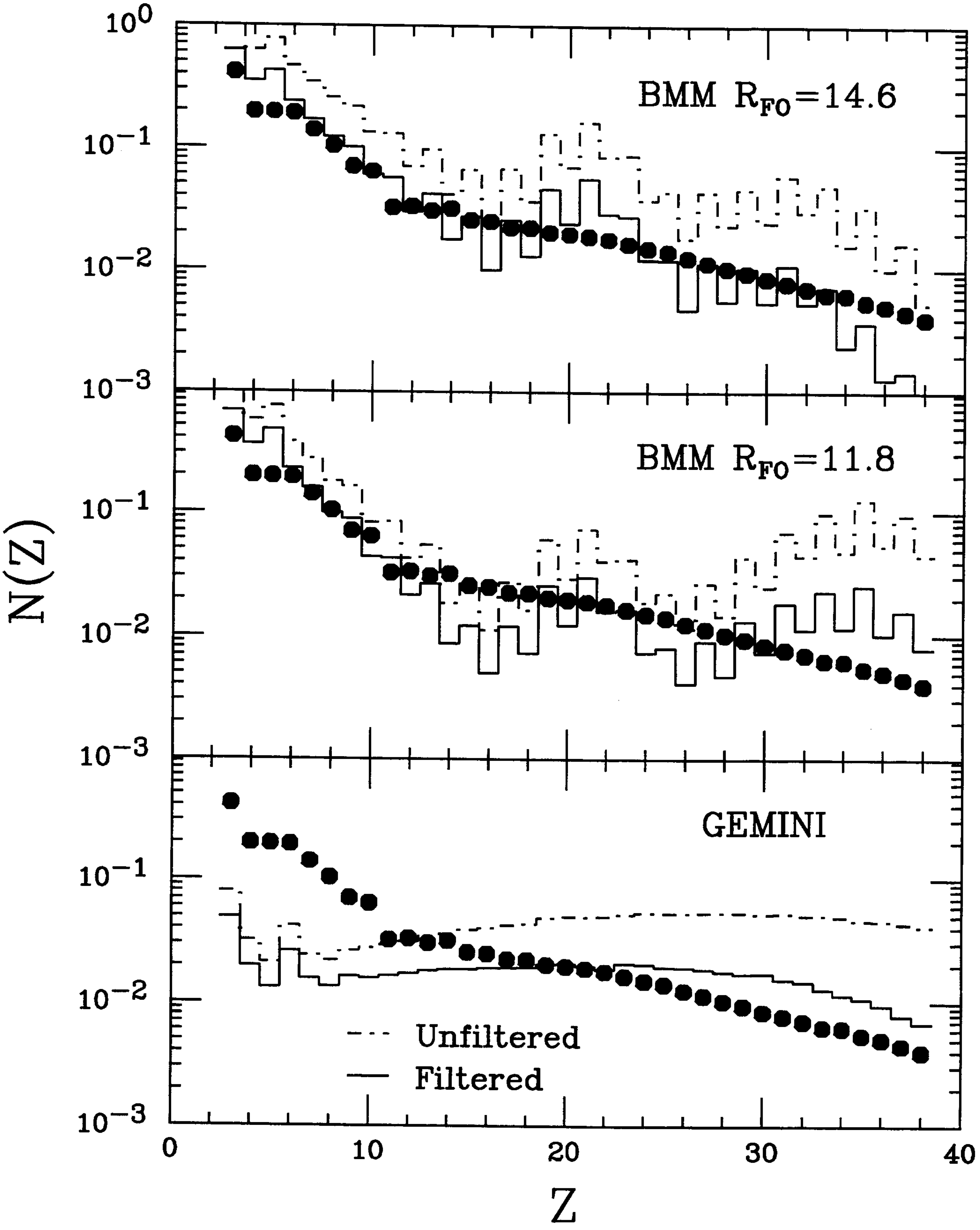
BMM R_{FO}=14.6
BMM R_{FO}=11.8
GEMINI
Unfiltered
Filtered
N(Z)
Z
10^0
10^{-1}
10^{-2}
10^{-3}
0
10
20
30
40

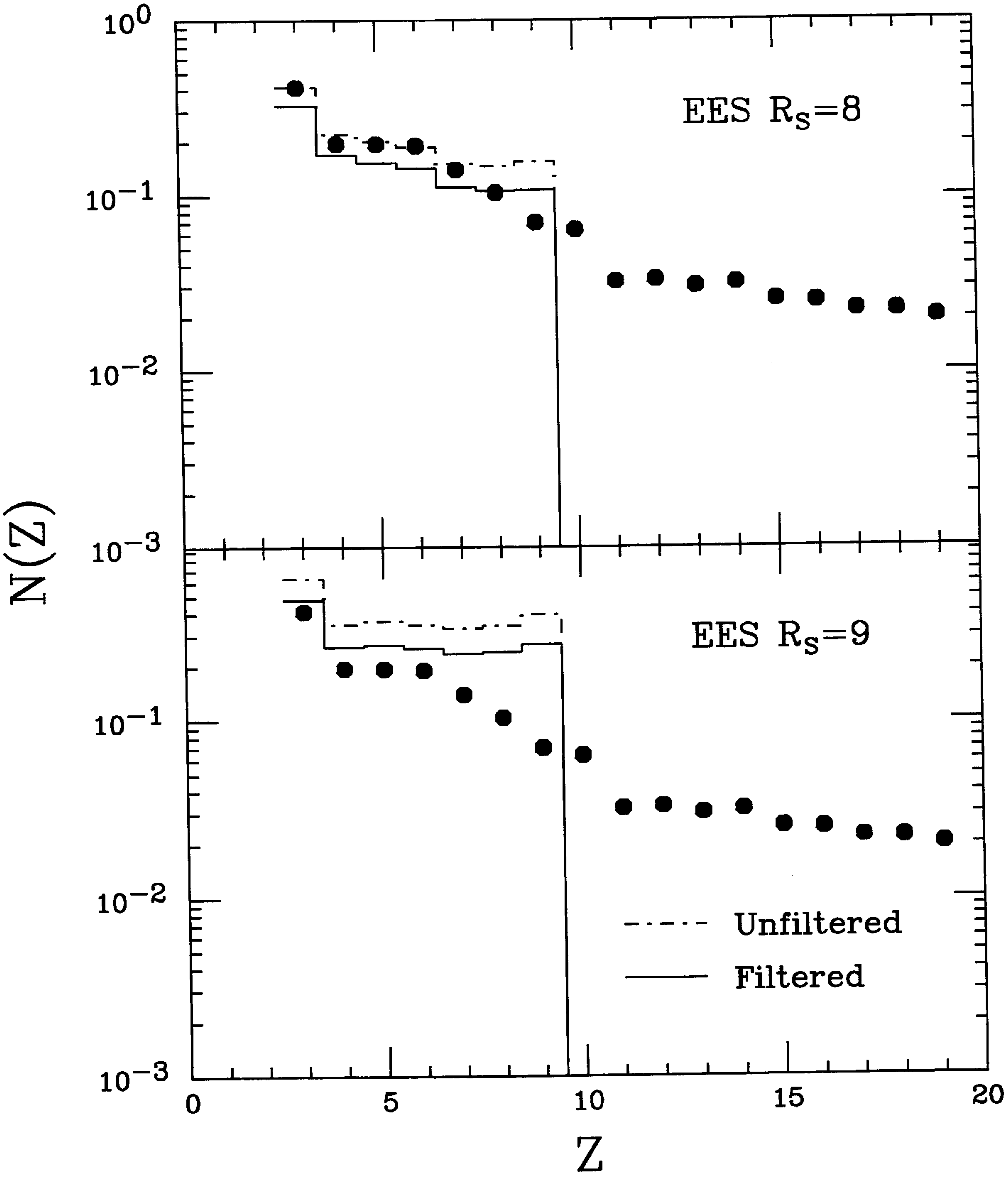
EES R_S=8
EES R_S=9
Unfiltered
Filtered
N(Z)
Z
10^0
10^{-1}
10^{-2}
10^{-3}
0
5
10
15
20

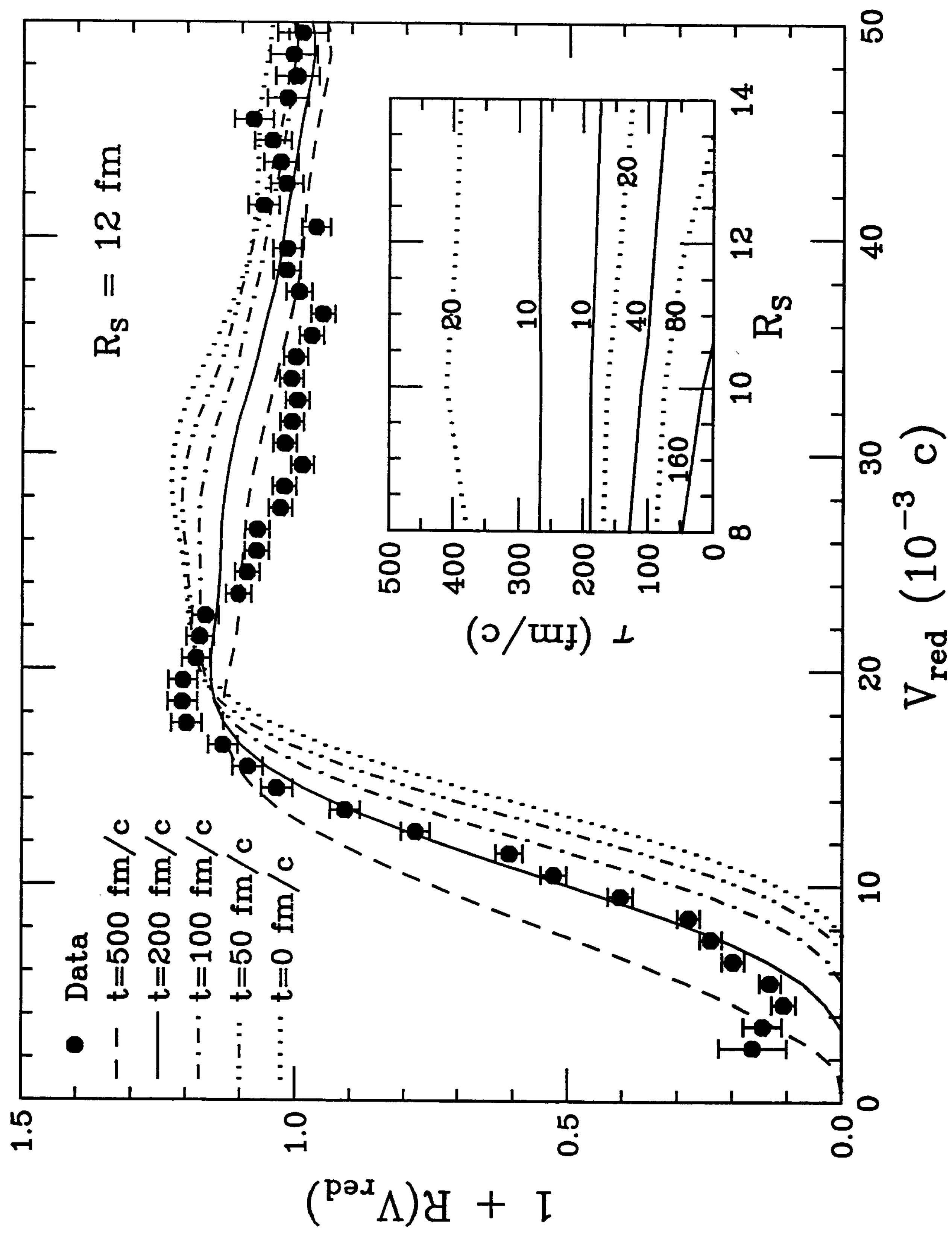

R_S = 12 fm
Data
t=500 fm/c
t=200 fm/c
t=100 fm/c
t=50 fm/c
t=0 fm/c
1 + R(V_red)
0.0
0.5
1.0
1.5
V_red (10^-3 c)
0
10
20
30
40
50
τ (fm/c)
0
100
200
300
400
500
R_S
8
10
12
14
20
10
10
40
80
160
20

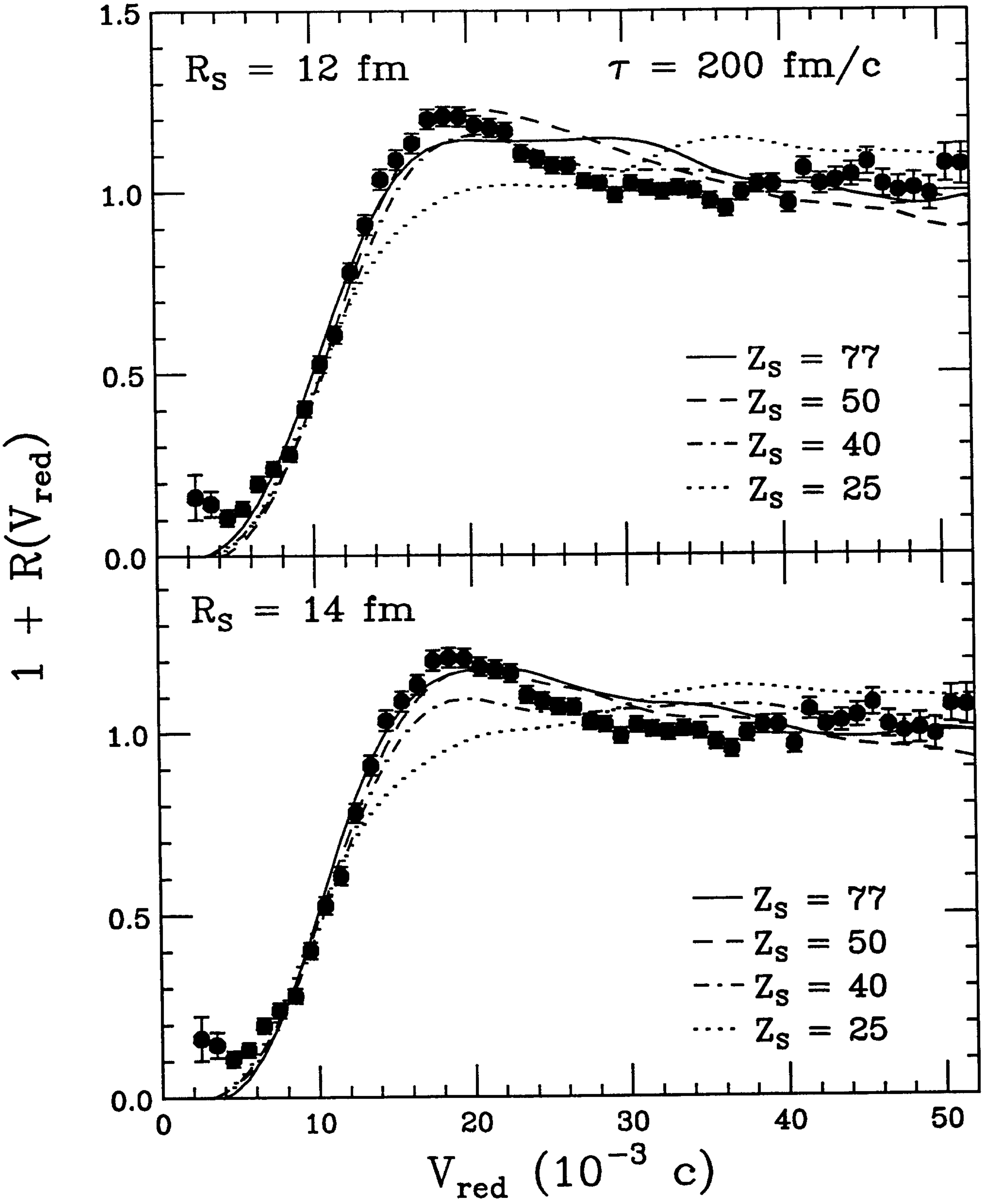

R_S = 12 fm
τ = 200 fm/c
R_S = 14 fm
Z_S = 77
Z_S = 50
Z_S = 40
Z_S = 25
1 + R(V_{red})
V_{red} (10^{-3} c)
0.0
0.5
1.0
1.5
0
10
20
30
40
50

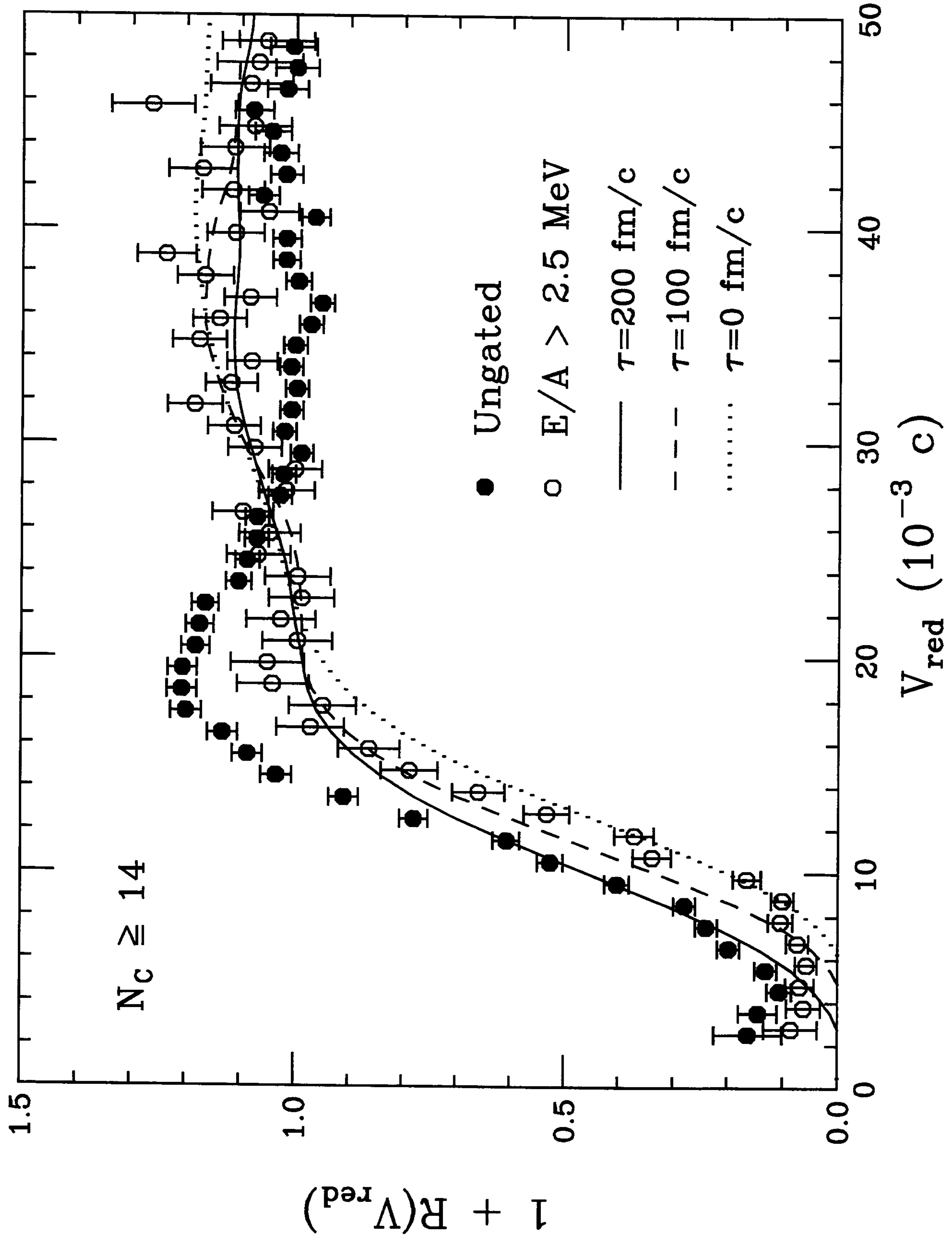
$N_C \geq 14$
● Ungated
○ E/A > 2.5 MeV
—— τ=200 fm/c
– – – τ=100 fm/c
······ τ=0 fm/c
V_{red} (10^{-3} c)
0
10
20
30
40
50
1 + R(V_{red})
0.0
0.5
1.0
1.5

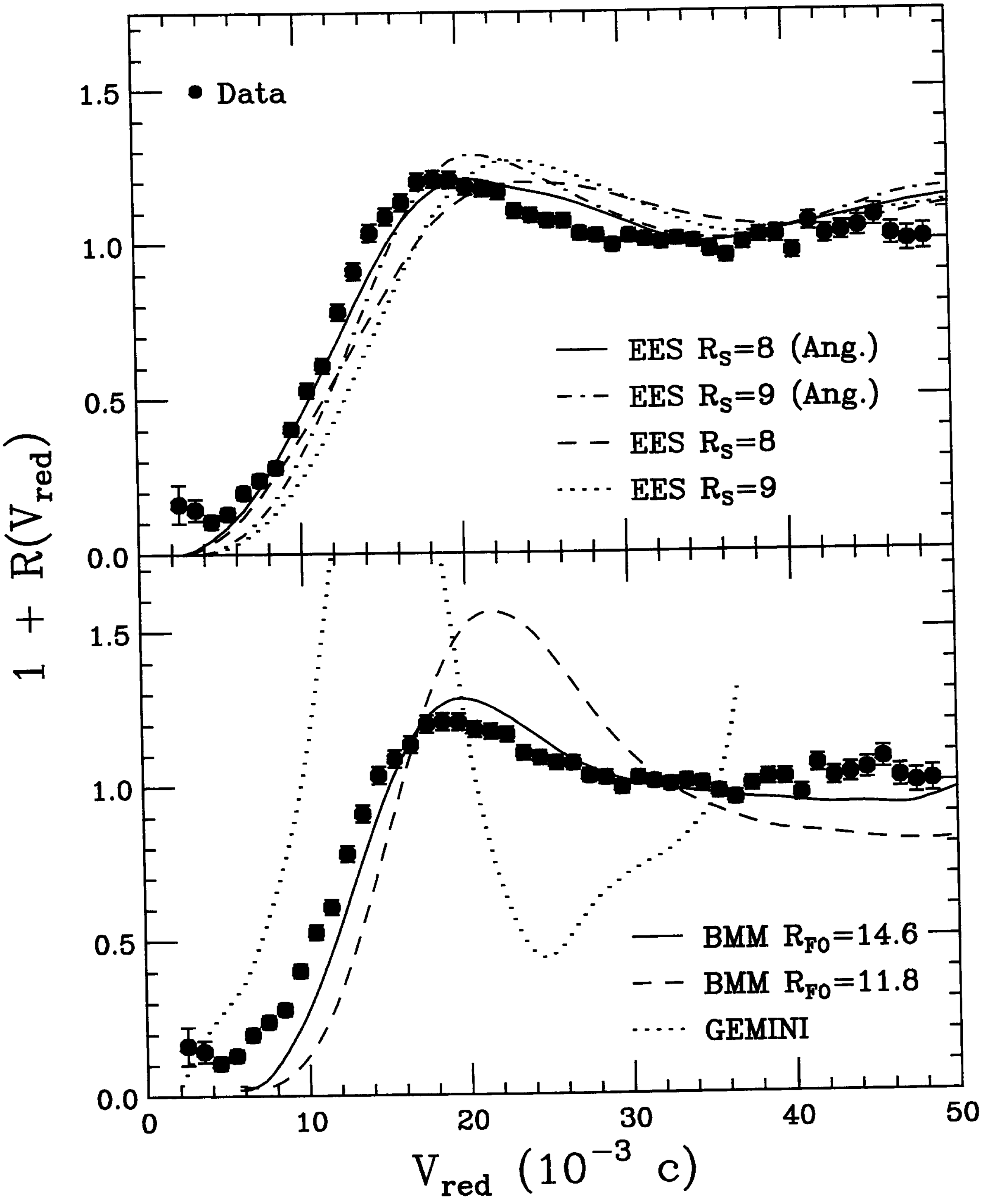
● Data
EES R_S=8 (Ang.)
EES R_S=9 (Ang.)
EES R_S=8
EES R_S=9
BMM R_{FO}=14.6
BMM R_{FO}=11.8
GEMINI
1 + R(V_{red})
V_{red} (10^{-3} c)
0.0
0.5
1.0
1.5
0
10
20
30
40
50

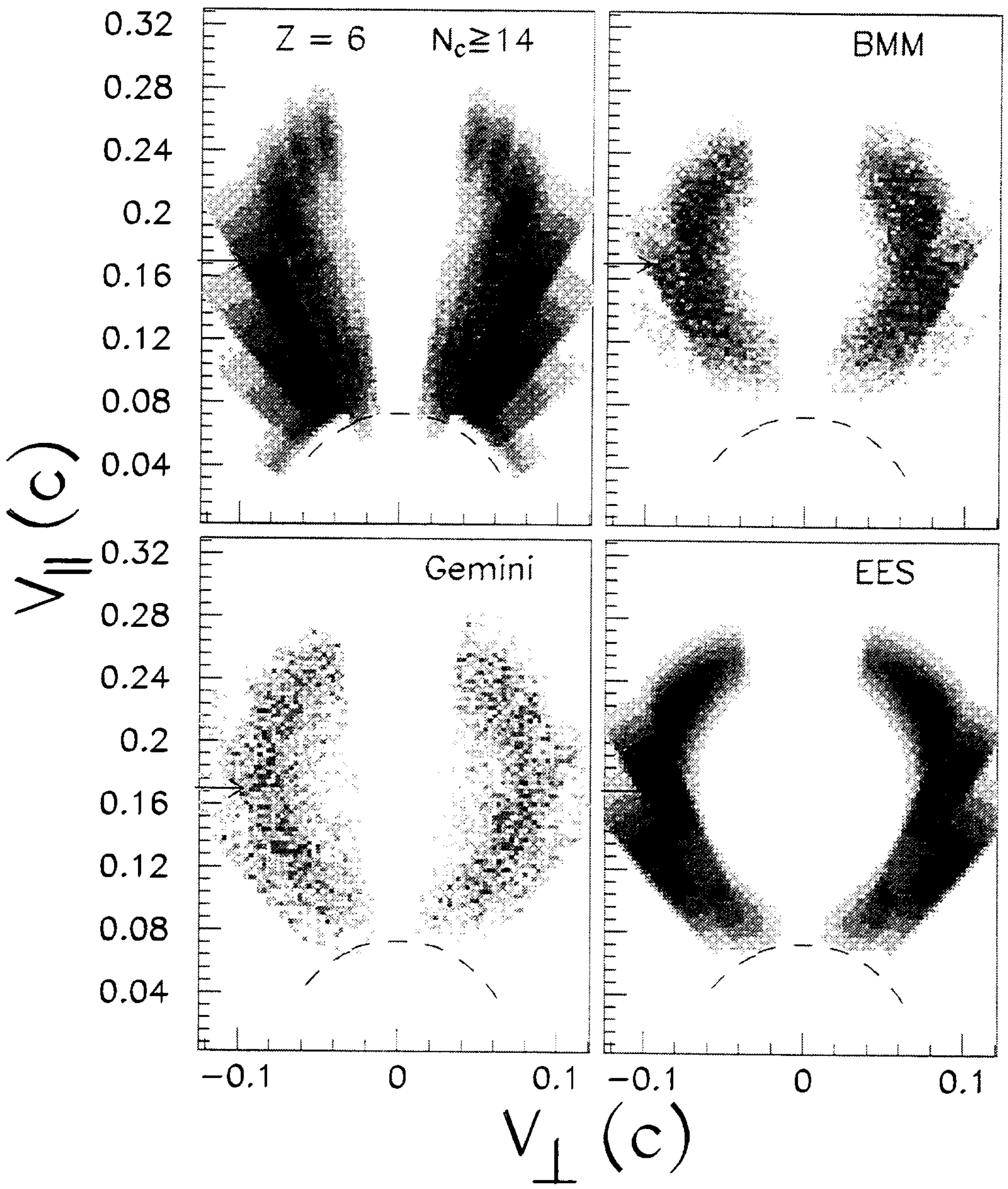
Z = 6
$N_c \geq 14$
BMM
Gemini
EES
0.32
0.28
0.24
0.2
0.16
0.12
0.08
0.04
$V_{\parallel}$ (c)
−0.1
0
0.1
$V_{\perp}$ (c)

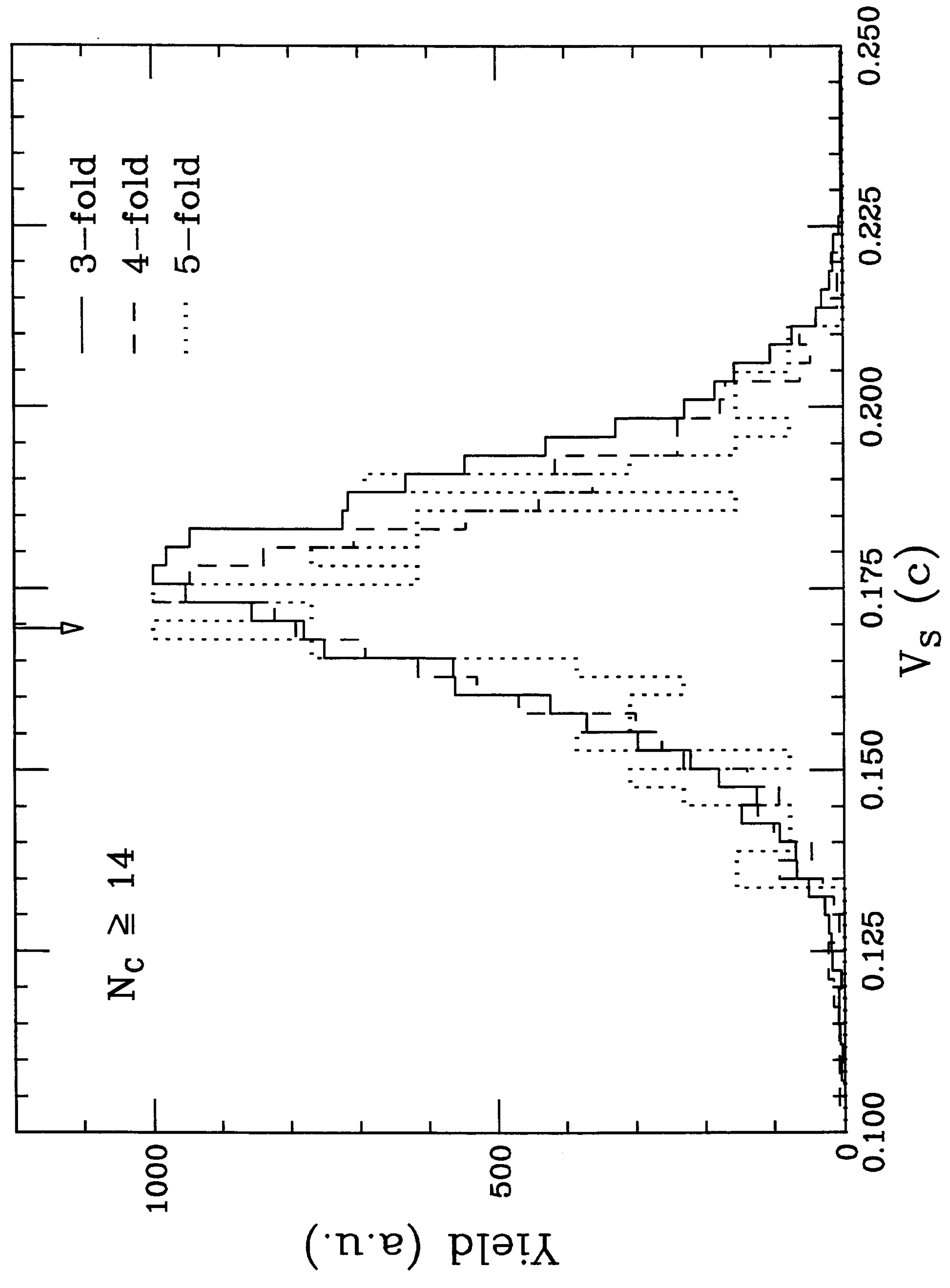

$N_C \geq 14$
3−fold
4−fold
5−fold
Yield (a.u.)
0
500
1000
V_S (c)
0.100
0.125
0.150
0.175
0.200
0.225
0.250

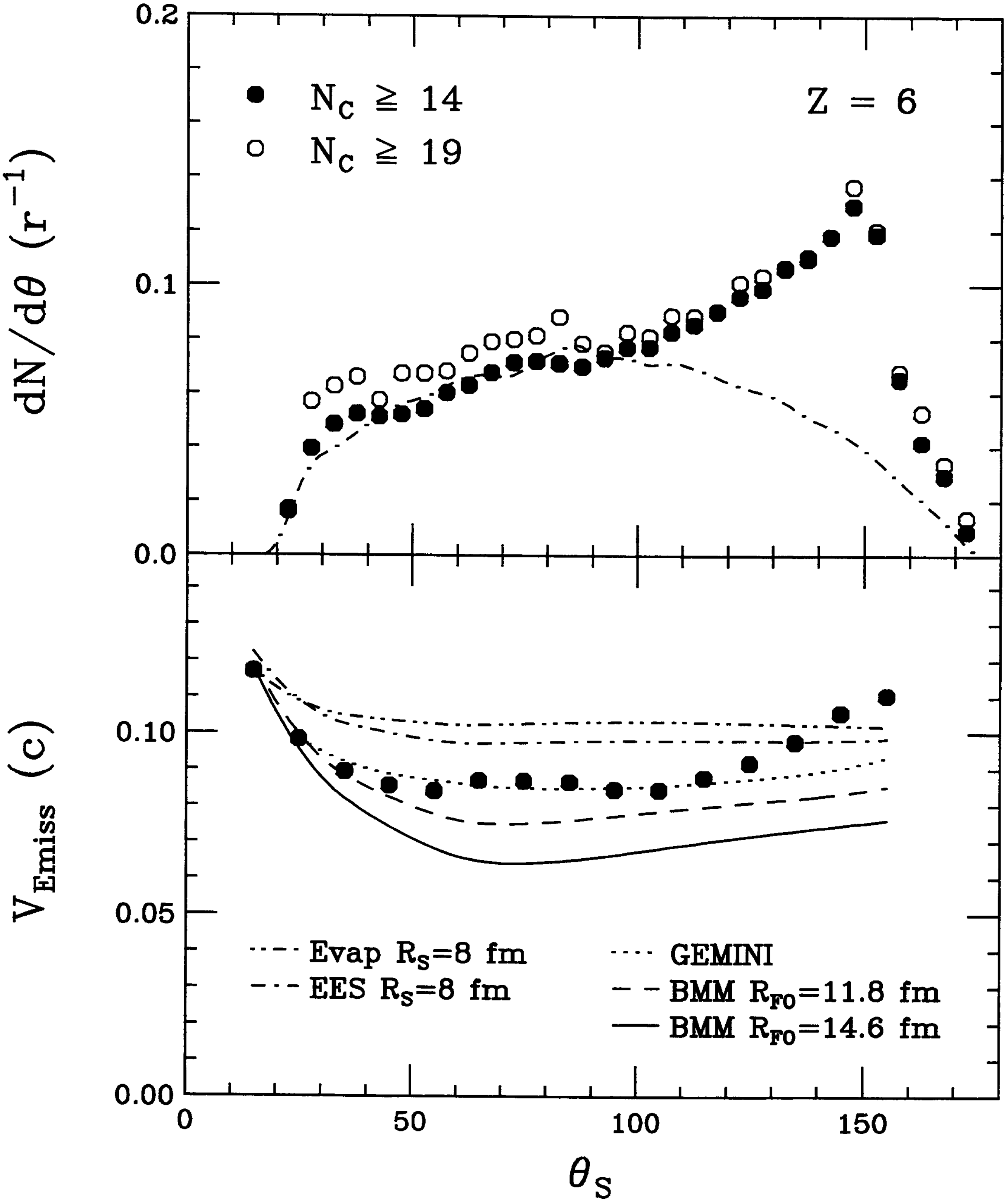

0.2
0.1
0.0
dN/dθ (r⁻¹)
● N_C ≧ 14
○ N_C ≧ 19
Z = 6
0.10
0.05
0.00
V_Emiss (c)
Evap R_S=8 fm
EES R_S=8 fm
GEMINI
BMM R_FO=11.8 fm
BMM R_FO=14.6 fm
0
50
100
150
θ_S